# Screening hydrotreating catalysts for the valorization of a light cycle oil/ scrap tires oil blend based on a detailed product analysis

Roberto Palos[a], Timo Kekäläinen[b], Frank Duodu[b], Alazne Gutiérrez[a], José M. Arandes[a], Janne Jänis[b], Pedro Castaño[a,c,*]

[a] Department of Chemical Engineering, University of the Basque Country UPV/EHU, PO Box 644, 48080, Bilbao, Spain
[b] Department of Chemistry, University of Eastern Finland, PO Box 111, FI-80101, Joensuu, Finland
[c] Multiscale Reaction Engineering, KAUST Catalysis Center (KCC), King Abdullah University of Science and Technology (KAUST), Thuwal, 23955-6900, Saudi Arabia

ABSTRACT

Predicting the hydrotreating performance of industrial catalysts used for upgrading heavy oils is hampered by the unknown chemistry behind it. In this work, we have used a set of chromatographic and mass spectrometric techniques (APPI/ESI FT-ICR MS, FID-MS GC × GC and PFPD GC) for acquiring a more precise composition of the feed and products of the hydrotreatment of a blend of light cycle oil and scrap tire oil (20 vol%) using three benchmark catalysts: CoMo/Al$_2$O$_3$, NiMo/SiO$_2$-Al$_2$O$_3$ and NiW/USY zeolite. Despite the different nature of the catalysts, the composition of the products was relatively similar, indicating the slower and controlled trans- formation of the heaviest molecules of the feed, particularly in tire oil. A faithful analysis of these molecules by combining the results of the analysis clarifies the multiple mechanisms affecting hydrotreating simultaneously: hydrodearomatization, hydrocracking, hydrodesulfurization, hydrodeoxygenation and hydrodenitrification. An effort has been made to use these results in a quantitative manner for catalyst screening.

## 1. Introduction

Nowadays, oil refineries are facing several challenges due to the continuous decrease in the quality of used petroleum, the necessity to intensify the refining capacity and the increasingly strict environmental laws affecting fuel composition [1]. Consequently, refineries are ex- panding their activity towards new actions, in particular to the in- corporation of non-conventional feeds, such as refinery secondary streams [2,3], vegetal biomass derived streams [4,5] and wastes from the consumers society [6,7]. In this context is where waste-refinery, defined as the integrated technologies that process and co-process re- sidual waste streams, becomes an important initiative for extending the lifetime and enhance the margins of the refineries.

Within the wastes with potential implementation in the waste-re- finery, tires are of special interest due to their yearly volume dumped, environmental damage and prospective composition from where high- quality fuels can be obtained [8]. Scrap tires should be submitted to a pyrolysis stage in order to obtain a liquid product that is easily ma- nipulated or upgraded in the refinery [9], commonly known as scrap tire oil (STO). From the point of view of its potential as a fuel, STO has a higher heating value of 41–44 MJ kg$^{-1}$, it is chemically stable, and it has a high concentration of fractions such as gasoline and middle

distillates (boiling points = 130–350 °C). On the other hand, the gasoil fraction of STO has a very low cetane index (ca. 17.6), the gasoline fraction has high content of aromatics (ca. 65 wt% in total) and a very high content of heteroatoms, e.g., sulfur and nitrogen (ca. 14000 and 4100 ppm, respectively) [10].

Considering the conventional processes available in refineries, hy- droprocessing appears as the most suitable one to upgrade STO and other waste streams [11]. Hydroprocessing refers to two separated processes [12–14]: hydrotreating and hydrocracking. Hydrotreating aims at removing undesired impurities such as sulfur, nitrogen, oxygen, aromatics and metals, leading to the desired pathways of reaction: hydrodesulfurization (HDS), hydrodenitrogenation (HDN), hydro- deoxygenation (HDO), hydrodearomatization (HDA) and hydro- demetallization (HDM). On the other hand, hydrocracking (HC) trans- forms low value heavy oil fractions into highvalue middle distillates using harsher conditions than hydrotreating. Regardless of the type of hydroprocessing, catalysts are mostly based on supported transition metals. Despite the composition of these catalysts may seem unchanged over the past decades, a great incremental performance has been ob- served [15,16]. The latest advances of hydroprocessing catalysts are, for example, synthesizing ultrafine MoNiS and MoCoS monolayers [17], incorporating carbides [18] or carbon-based materials [19,20] within

---

the catalyst structure or adapting new metallic precursors [21]. In fact, many catalyst manufacturers compete in the very demanding field of hydroprocessing, with dozens of different applications to satisfy the demanding market. Within a large portfolio of possible feeds and products, the selection of the best catalyst has been long a topic of debate, trying to define parameters to easily assess and predict this catalytic performance on the grounds of feed properties [22].

The problem associated with catalyst screening in hydroprocessing is the complexity of the process which involves thousands of molecules, hundreds of reaction pathways, several phases, deactivation and dynamic catalytic surface, among others. Thus, extracting intrinsic kinetic or catalytic information out of real feed is relatively difficult. Traditionally, this issue has been solved using representative model compounds. This approach is acceptable to select the best catalyst candidate but it is totally unreliable to predict the catalyst performance for STO hydroprocessing [6]. Thus, in such complex reaction networks, catalyst structure-activity correlations are hindered by the limitations to define the "activity", and because catalyst performance drops orders of magnitude, making impossible to stablish direct correlations [6]. All in all, a fundamental understanding of the effect of catalyst structure on activity should be performed with model components, but any application of these catalysts requires an understanding of the complex kinetics involved. In this last point and with the advance of analytical techniques and computer-aided analysis of the data, new horizons are opening for extracting this particular intrinsic kinetic or catalytic information [23]. In this sense, ultrahigh-resolution Fourier transform ion cyclotron resonance mass spectrometry (FT-ICR MS) has made a great impact on petroleomics [24,25] by being able to characterize complex mixtures, such as heavy oil feeds [26–28] or biomass derived streams [29–31]. In particular, FT-ICR MS is making a great impact in solving the mechanisms of complex catalytic systems, such as fluid catalytic cracking [32], hydrodemetallization [33] or hydrodenitrogenation [34–36]. For example, Zhang et al. [37] performed a screening of NiMo, NiW and CoMo supported catalysts within the shale oil hydrotreatment by using FT-ICR MS. Based on the results, NiMo catalyst showed the best performance in HDS and HDN. However, a more quantitative approach is required in order to standardize the analytical methodology, especially the use of different ionization methods, like electrospray ionization (ESI) and atmospheric pressure photoionization (APPI), which seems very important according to the previous results [38–40].

In this work, we have used a set of analytical techniques (APPI/ESI FT-ICR MS, FID-MS GC × GC and PFPD GC) for acquiring a detailed composition of the feed and products during the hydroprocessing of a blend of light cycle oil (LCO, a conventional secondary refinery stream) and scrap tire oil (STO, 20 vol%). Several hydroprocessing catalyst have been characterized and tested in the reaction: CoMo/Al$_2$O$_3$, NiMo/SiO$_2$–Al$_2$O$_3$ and NiW/USY zeolite. Then, the detailed analytical composition of feed and products has been used to quantify the main reaction pathways of the reaction: HDS, HDN, HDO, HDA and HC. This has been done in a collective way or analyzing individual types of molecules in order to evaluate the catalytic activity of each system within the multiple reaction pathways occurring simultaneously.

## 2. Experimental

### 2.1. Catalysts characterization

Three commercial catalysts have been used in the hydrotreatment of the STO/LCO blend: CoMo/Al$_2$O$_3$, NiMo/SiO$_2$–Al$_2$O$_3$ and NiW/USY zeolite. These have been named as CoMo/ALM, NiMo/ASA and NiW/USY, respectively. The catalysts have been characterized by means of several techniques: (i) the metal content of the catalysts was determined by means of ICP-AES with a X7-II Thermo Elemental quadrupole mass spectrometer (Q-ICP-MS), provided with Xt interface and concentric nebulizer; (ii) the textural properties were analyzed with N$_2$ adsorption-desorption isotherms obtained at −196 °C in a

Micromeritics ASAP 2020, after 8 h of degasification at 150 °C. Specific surface was calculated using the BET equation, pore volume using t-method and pore size distribution and average pore diameter were estimated by BJH method; (iii) the acidic properties were determined in a Setaram DSC thermogravimetric-calorimeter analyzer coupled on-line to a Balzers Quadstar 422 mass spectrometer by temperature programmed desorption (TPD) up to 500 °C, of *tert*-butylamine (t-BA) previously adsorbed at 100 °C. Moreover, the Brønsted to Lewis acid site ratio (BAS/LAS) has been determined by FTIR spectroscopy of pre-adsorbed pyridine on catalyst wafer in a Nicolet 740 SX. The BAS/LAS has been calculated from the vibrational bands of pyridine adsorbed at 1547 and 1455 cm$^{-1}$, associated with Brønsted and Lewis sites, respectively; (iv) the morphology at the nanoscale were determined by transmission electron microscopy (TEM), which have been performed using a SuperTwin CM200 Philips microscope (acceleration voltage, 200 kV; resolution, 0.235 nm) equipped with a lanthanum hexaboride filament and EDX microanalysis system. Each sample preparation began by the dispersion in hexanol, followed by deposition and extension of a drop of the solution on a 300 mesh copper grid, coating with a porous carbon film and, drying of the sample under vacuum.

### 2.2. Hydrotreating unit and conditions

The runs have been carried out in a fixed bed reactor working with continuous feeding of the blend STO/LCO, in the trickle-bed regime. The unit has been extensively described in previous works [41,42]. The operation conditions have been the following: temperature, 400 °C; pressure, 80 bar; weight hourly space velocity (WHSV), 5 h$^{-1}$; H$_2$:oil ratio, 1000 Ncm$^3$ cm$_{oil}^{-3}$; and time on stream (TOS), 8 h. Before the reaction, the catalysts have been sulfided *in-situ* in a gaseous stream of 50 cm$^3$ min$^{-1}$ of H$_2$S:H$_2$ (10 vol%) mixture flow, at 400 °C during 4 h. With the aim of favoring plug flow regime and avoiding temperature gradients within the catalyst bed, the catalyst has been mixed with silicon carbide according to the protocol described by Van Herk et al. [43].

### 2.3. Analysis of feeds and products

The light cycle oil (LCO) used in this work is a byproduct of the catalytic cracking unit (FCC) of the refinery located in Muskiz (Biscay, Spain). The scrap tire oil (STO) has been produced using a conical spouted bed reactor in a laboratory pyrolysis plant at 500 °C following the procedure previously described by Lopez et al. [9]. The STO/LCO blend has been prepared mixing the proper amounts of liquids in order to reach 20 vol% of STO. This value has been chosen by accounting the standard capacity of an LCO hydrotreating unit and the potential production of STO by delocalized pyrolysis units.

Physicochemical properties of the feeds were determined according to standard procedures: density was determined according to ASTM D 4052 Standard and simulated distillation was carried out in an Agilent 6890 gas chromatograph provided with a DB-2887 semi-capillary column (dimethylpolysiloxane, 10 m, 0.53 mm, 3.00 μm) following the procedure detailed in ASTM D 2887 Standard. Elemental analysis of the feeds (C-H-N) was carried out in Euro EA Elemental Analyzer, sulfur content was measured in a separate module (TruSpec S) and the amount of oxygen was obtained by difference.

For the characterization of the feeds and the reaction liquid products, comprehensive two-dimensional GC (FID-MS GC × GC) was applied, as described in previous works [6,7]. The system consists of an Agilent 7890 gas chromatograph equipped with a flow modulator between primary and secondary columns. Primary column was a nonpolar DB-5MS capillary column (5% phenyl methylpolysiloxane, 30 m, 0.25 mm, 0.25 μm) and secondary column was a polar HP-INNOWax capillary column (polyethylene glycol, 5 m, 0.25 mm, 0.5 μm). It was either equipped with a FID detector and with an inert XL MSD detector (5975C Mass Spectrometer). This equipment analyzes simultaneously

each sample under MS and FID, so any assignment performed was verified using the mass spec data prior the quantification.

Speciation of the sulfur compounds has been done in an Agilent 7890A gas chromatograph equipped with both FID and PFPD detectors. The separation was performed on a HP-PONA capillary column (50 m, 0.20 mm) coated with dimethylpolyisiloxane (film thickness, 0.50 μm).

For the FT-ICR MS experiments, the sample oils were dissolved in toluene-methanol mixture (1:1 v/v) to the concentration of 100 μg cm$^{-3}$ for positive-ion (+)APPI analysis and in methanol to 50 μg cm$^{-3}$ for (+)ESI analysis, respectively. All the used solvents were HPLC grade. All mass spectrometry experiments were performed using a 12-T Bruker solariX XR FT-ICR mass spectrometer (Bruker Daltonics, Bremen, Germany), equipped with a dynamically harmonized Paracell ICR cell and an Apollo-II atmospheric pressure ion source, operating both APPI and ESI. The sample introduction to the ion source was done via a syringe pump at a flow rate of 2·10$^{-3}$ cm$^3$ min$^{-1}$. For APPI, the sample was delivered at a flow rate of 7·10$^{-3}$ cm$^3$ min$^{-1}$ through the heated nebulizer operated at 400 °C under nitrogen sheath gas at 50 psi with the auxiliary port being plugged. Dry nitrogen was used as drying and nebulizing gas. The generated ions were accumulated in the hexapole ion trap and transferred to the ICR cell for trapping, excitation and detection. The data acquisition program used was Bruker Compass ftmsControl 2.1 software.

For each spectrum, a broadband frequency excitation and detection was carried out by using 300 co-added 8 MWord time-domain transients, which were summed, full-sine apodized and zero-filled once to provide final 16 MWord magnitude-mode data spanning m/z range of 100–2000. External mass calibration of all FT-ICR spectra was done using sodium trifluoroacetate (STFA) clusters [44] for the ESI measurements and APCI-L tuning mix (Part No. G1969-85010, Agilent Technologies) for the APPI experiments. The internal re-calibration was made with respect to the known hydrocarbon (HC) class species for the APPI and the N$_1$ / O$_x$ class species for the ESI data.

For the molecular formula assignment, the parameters were set as follows: double bond equivalent (DBE) 0–80; mass error ± 1.0 ppm; atomic formula $^{12}C_{1-100}{}^{1}H_{1-200}{}^{14}N_{0-4}{}^{16}O_{0-12}{}^{32}S_{0-4}{}^{22}Na_{0-1}$ ($^{13}$C and $^{34}$S isotopes were taken into account with the nitrogen rule being followed). The peaks with signal-to-noise (S/N) ≥ 5 were taken into account. The data post-processing and molecular formula assignments were carried out with DataAnalysis 5.0 software (Bruker Daltonics). The homologous series for each heteroatom class (members of the same class but a varying carbon number, C#) were tabulated according to their respective relative abundance and DBE using Microsoft Excel (Microsoft Corporation). For all compounds, both molecular ions (M$^{+\bullet}$) and protonated molecules ([M + H]$^+$) were observed with (+)APPI; however, since the relative intensity for M$^{+\bullet}$ was over 80% for the most abundant compound classes, the data have been presented for the radical ions only. With (+)ESI, either [M + H]$^+$ or [M + Na]$^+$ ions were observed. DBE indicates the number of rings and double bonds (degree of unsaturation) of a specific molecule and was calculated as follows:

$$DBE(C_cH_hN_nO_oS_s) = c - \frac{h}{2} + \frac{n}{2} + 1 \qquad (1)$$

Note that M$^{+\bullet}$ ions have integer DBE, while [M + H]$^+$ ions have non-integer DBE, and can thus be easily distinguished.

## 3. Results

### 3.1. Catalyst properties

Attending to the content of metals in the catalysts, it can be seen in Table 1 that all of them have the typical metal concentrations of both the main phase (Mo or W) and that of the precursor (Co or Ni). NiW/

**Table 1**
Metal content of the fresh catalysts measured by means of ICP-AES.

| Catalyst | CoMo/ALM | NiMo/ASA | NiW/USY |
|---|---|---|---|
| Co (wt%) | 2.83 | – | – |
| Mo (wt%) | 12.2 | 7.31 | – |
| Ni (wt%) | – | 2.98 | 4.54 |
| W (wt%) | – | – | 22.7 |

USY catalyst stands out with the greatest main phase concentration (22.7 wt% of W), with a value twice and three times higher than that of the other catalysts. Fig. 1 shows the main textural (Fig. 1a) and acidic (Fig. 1b) features of the catalysts employed. Focusing on textural properties, the values of the surface area (S$_{BET}$) are partially correlated with the micropore area (S$_M$) and at the same time, with the average pore size: NiW/USY has the highest S$_{BET}$ (317 m$^2$ g$^{-1}$) and S$_M$ (184 m$^2$ g$^{-1}$), while the smallest pore size (4.3 nm), NiMo/ASA has the intermediate values of S$_{BET}$ (208 m$^2$ g$^{-1}$), S$_M$ (45 m$^2$ g$^{-1}$) and pore size (7.4 nm) and on the other side, CoMo/ALM has the lowest S$_{BET}$ (144 m$^2$ g$^{-1}$) and S$_M$ (4 m$^2$ g$^{-1}$), while the biggest pore size (10.8 nm). On regard to the acidic features (Fig. 1b), the values of total acidity are partially correlated with the acidic strength and BAS/LAS: NiW/USY has the lowest acidity (0.405 mmol$_{t-BA}$ g$^{-1}$), while the greatest acidic strength (550 J mmol$_{t-BA}^{-1}$) and BAS/LAS (2.39), NiMo/ASA has the intermediate values of acidity (0.458 mmol$_{t-BA}$ g$^{-1}$), acidic strength (534 J mmol$_{t-BA}^{-1}$) and BAS/LAS (2.25) and on the other side, CoMo/ALM has the greatest acidity (0.542 mmol$_{t-BA}$ g$^{-1}$), while the lowest acid strength (511 J mmol$_{t-BA}^{-1}$) and BAS/LAS (2.16). The metal loading could influence the total acidity of the catalyst [45], however given the different support natures and metallic loading, this correlation cannot be established. On the other hand, the number of BAS seems to be correlated with the acid strength of the catalyst (separated experiments) so that BAS can be identified with those sites of greater acid strength.

Fig. 2 shows the main features of the catalysts at the nanoscale using TEM imaging. CoMo/ALM (Fig. 2a) and NiMo/ASA (Fig. 2b) catalysts display a mesoporous texture with disordered distribution and a chaotic segregation of darker planes corresponding to piles of metals, i.e. mainly phases of Mo, which is the main metal on both catalysts (Table 1), after Co or Ni. NiW/USY catalyst (Fig. 2c) displays ordered microporous texture within zeolite crystals of about 400–700 nm and darker areas of Ni and W metallic phases. Upon sulfidation, all catalysts show the stacks of sulfide metallic phases of Mo or W. In this sense, NiMo/ASA catalyst (Fig. 2e) has a higher stacking degree than its counterparts: CoMo/ALM (Fig. 2d) and NiW/USY catalysts (Fig. 2f).

### 3.2. Properties of the feedstock

A detailed compositional analysis of the two individual constituents of the blending (LCO and STO) has been undertaken by means of combining the measurements of density, simulated distillation, elemental analysis, FID-MS GC × GC and APPI/ESI FT-ICR MS. Despite having identical densities (Table 2), the profiles of boiling of both LCO and STO are quite different (Table 2): the initial boiling points (IBP) are relatively similar (ΔT = 13.7 °C), but as the fraction distilled increases from 50 up to 95 wt% so it does the difference in boiling points (T$_{50}$ and T$_{95}$), with ΔT of 25.4 and 108.6, respectively. The final boiling point (FBP) difference is about 99.0 °C. This trend indicates that STO has a more heterogeneous composition with the presence of heavy and bulky molecules with boiling points higher than 380 °C and C# > 20, typical of the tars derived from the tire thermal cracking or pyrolysis. On the other hand, LCO is a distillation cut from the FCC fractionator, and
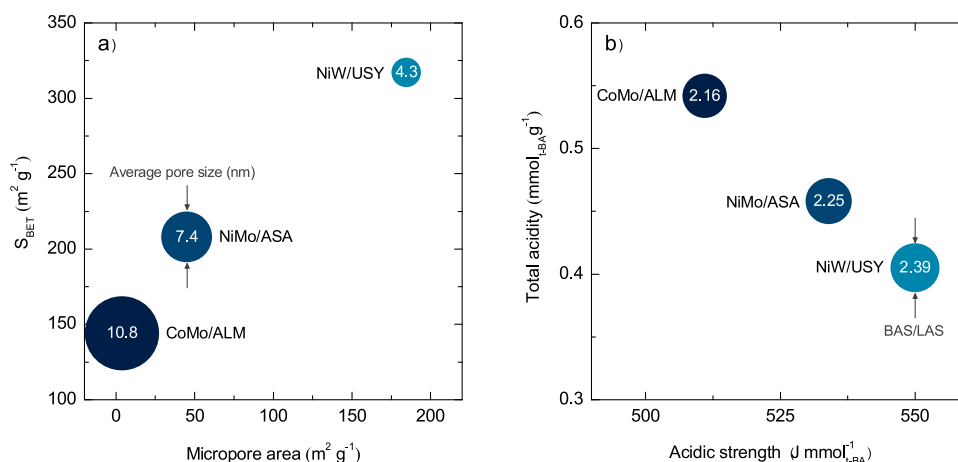
**Fig. 1.** Textural a) and acidic b) properties of used catalysts.

hence, the boiling point distribution is relatively narrower and lighter compared with STO. Taking the elemental composition of the feeds in Table 2, STO has a higher concentration of heteroatoms (sulfur, nitrogen and oxygen) than LCO, which turns out reactants for any further hydroprocessing reaction. As for the H/C ratio, there is not any significant difference between LCO and STO to explain the greater or lower insaturation degree of those feeds.

The results of the FID GC × GC and APPI FT-ICR MS of the individual blend constituents have been represented in Fig. 3a–b and Fig. 3c-d, respectively. These results represent the composition of LCO and STO within the region created by DBE and C# [46]. This type of graphs have been fruitfully used for the analysis of petroleum derived fractions [28,47], biomass derived pyrolysis oils [31,48], SARA

fractions [49,50] and scrap tire oil [51] among other applications.

Both FID GC × GC and APPI FT-ICR MS techniques have enough precision to resolve the structure of each hydrocarbon molecule or its heteroatomic counterpart (with $N_n$, $O_o$ or $S_s$). The color-coded abundance plots shown in Fig. 3 represent the summation of the abundance of molecules with the same combination of DBE and number of carbons. More specifically, Fig. 3c-d represent the fraction of molecules detected that do not have heteroatoms (n, o and s = 0) and are hydrocarbons, namely CH species. Additionally, the intensities in the abundance plots have been projected into the DBE or C# axes in order to obtain the bar plots represented in the same Fig. 3. The other main compound classes detected with APPI were $N_1$, $S_1$, and $O_{1-3}$. Also, a few minor compound classes, like $N_1O_{1-2}$, and $S_1O_1$, were also detected but not further
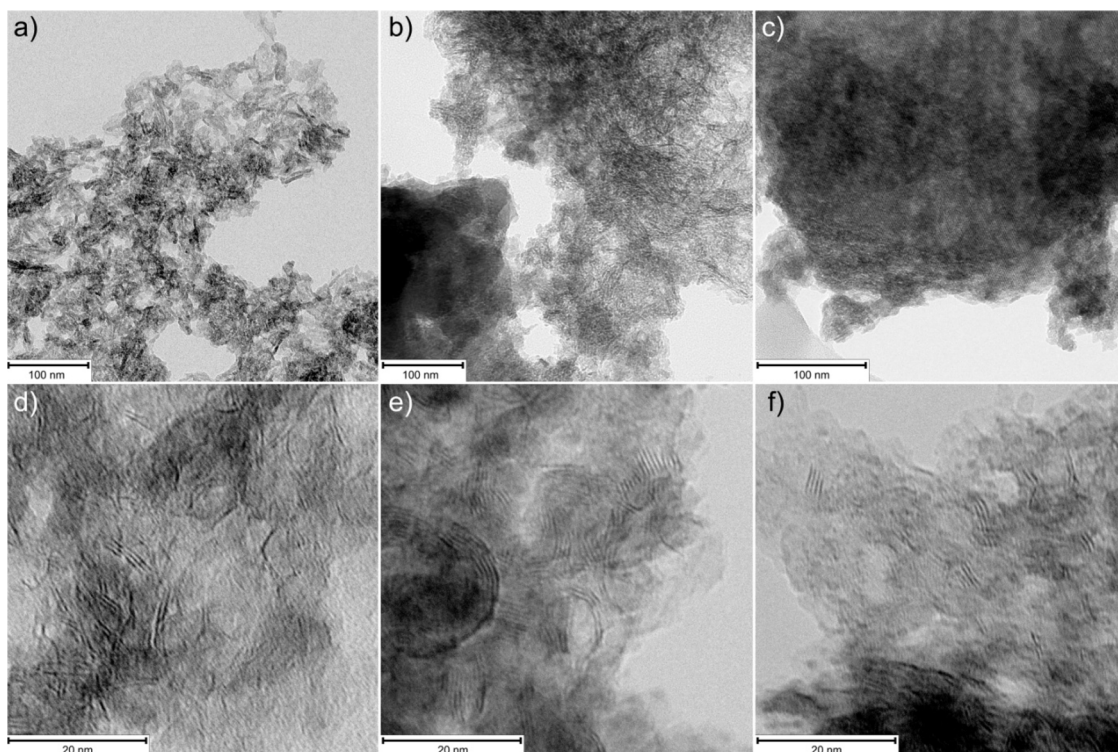


**Fig. 2.** TEM micrographs of the CoMo/ALM catalyst fresh a) and sulfided d); NiMo/ASA catalyst fresh b) and sulfided e); and, NiW/USY catalyst fresh c) and sulfided f).

**Table 2**

Main physicochemical properties of the LCO and STO. The standard deviation of all single values can be regarded as < 5%.

| | LCO | STO |
|---|---|---|
| Density, 15 °C (g mL) | 0.887 | 0.894 |
| Simulated distillation (SD) | | |
| IBP–FBP (°C) | 95.7–438.0 | 109.4–537.9 |
| $T_{50}$–$T_{95}$ (°C) | 288.6–381.3 | 314.0–489.9 |
| Elementary analysis (wt%) | | |
| C | 89.56 | 87.20 |
| H | 9.37 | 10.62 |
| S | 1.02 | 1.12 |
| N | 0.67 | 0.72 |
| O | 0.51 | 0.53 |
| FID GC × GC (wt%) | | |
| Paraffins | 34.25 | 38.17 |
| Naphtenes | 3.65 | 5.59 |
| Aromatics | 62.10 | 56.24 |
| 1-ring | 31.10 | 31.74 |
| 2-rings | 25.50 | 20.35 |
| 3-rings | 5.50 | 4.16 |
| APPI FT-ICR MS (abundance %) | | |
| Paraffins and naphtenes | 1.00 | 16.30 |
| Aromatics | 99.00 | 83.70 |
| 1-ring | 15.48 | 13.66 |
| 2-rings | 53.29 | 26.14 |
| 3-rings | 21.87 | 17.89 |
| 4-rings | 6.88 | 12.78 |
| $5^{+}$-rings | 1.49 | 13.22 |
| ESI FT-ICR MS (abundance %) | | |
| Paraffins and naphtenes | 2.48 | – |
| Aromatics | 97.52 | 100.00 |
| 1-ring | 7.47 | 12.89 |
| 2-rings | 40.55 | 46.48 |
| 3-rings | 14.20 | 24.45 |
| 4-rings | 32.05 | 16.18 |
| $5^{+}$-rings | 3.25 | – |
| PFPD GC (ppm) | | |
| Benzotiazol | – | 3663 |
| BT | 344 | – |
| $M_1$BT | 1414 | – |
| $M_2$BT | 2204 | – |
| $M_3$BT | 2641 | – |
| DBT | 208 | 176 |
| $M_1$DBT | 1093 | 726 |
| $M_2$DBT | 1255 | 3341 |
| $M_3$DBT | 981 | 3294 |
| Sulfur | 10,212 | 11,200 |

discussed here.

The results of FID GC × GC (Fig. 3a, c) indicate that LCO has a narrow distribution of species with C# = 8–18 with a maximum in C# = 11–12, whereas, STO has a broader distribution of species within C# = 6–25 and without a clear maximum. As for the DBE, LCO shows three maxima with values of 0, 4 and 7, which correspond to paraffins (*n*-paraffins or isoparaffins), 1- and 2-ring aromatics, respectively. In the case of STO, two maxima are observed, those corresponding to paraffins and 1-ring aromatics, being the concentration of the paraffins about 3 times bigger than that of monoaromatics. The results of APPI FT-ICR MS (Fig. 3d, f) indicate a bimodal carbon number distribution of species in the LCO with a maximum at C# = 15–16, observing a displacement of C# = 4 with regard to the results obtained with the FID GC × GC. On its side, STO shows a bimodal distribution with a maximum in C# = 20–24, also heavier than the distribution obtained by FID GC × GC. With regard to the degree of unsaturation, LCO shows

three maxima at DBE values of 4, 7–8 and 10, corresponding to 1-, 2 and 3-ring aromatics, respectively; while, STO shows a unimodal distribution centered in a DBE value of 10. Both samples (LCO and STO) have very similar densities and amount of aromatics, as observed in Table 1. Thus, we could not correlate between these two parameters.

Thereupon, comparing the results of each of the feeds and using different techniques, it is clear that there is a big difference between the data obtained with each technique. Note the singular scales of the of FID GC × GC and APPI FT-ICR MS graphs. This difference in the analysis is due to the fact that FID GC × GC is more sensitive to analyze lighter and paraffinic species, while APPI FT-ICR MS is more sensitive to analyze bulkier and condensed-aromatic species because the low mass cut-off and poor ionization efficiency restrict the use of FT-ICR MS at this mass range [52,53]. The results provided by the FID GC × GC with the FID are qualitative for the CH species, which is the most abundant class, and makes the techniques very useful for acquiring a more realistic view of the constituents [54] up to species with C# of 28 and DBE of 10. Approaching quantitative results by APPI FT-ICR MS is a recurrent issue which depends on several aspects, mainly the nature of the species to be detected and possible presence of interfering matrix compounds (i.e., ion suppression effects). Among the common ionization techniques within FT-ICR MS, APPI has been shown to possess less problems in these regards [55]. On the other hand, the molecular resolution of APPI FT-ICR MS, by means of number of species detected, is several orders of magnitude higher than FID GC × GC, reaching the detection of species with C# up to 50 and DBE up to 25.

The chemical group distribution shown in Table 2 has been obtained from the integration of the results plotted in Fig. 3a, c. Table 2 shows the chemical group distribution of the feeds obtained by means of multiple techniques: density, simulated distillation (SD), elementary analysis, FID GC × GC, APPI/ESI FT-ICR MS, and PFPD GC. The results of the FID GC × GC demonstrate that LCO contains 34.25 wt% paraffins, 3.65 wt% naphthenes and 62.1 wt% aromatics, whereas STO contains 38.17 wt% paraffins, 5.59 wt% naphthenes and 56.24 wt% aromatics. The results of APPI/ESI FT-ICR MS corroborate the fact that STO is heavier in terms of carbon number (Fig. 3) and boiling point (Table 2) than STO.

As listed in Table 2, elemental sulfur accounts for 10,212 ppm on LCO and 11200 ppm on STO. Although their elemental composition is quite similar, the sulfur species that can be found in LCO and STO are rather different. LCO contains the common sulfur compounds that are usually found in this type of refinery streams: (i) reactive compounds in HDS formed by benzothiophene (BT) and its alkyl homologues ($M_x$BT); and (ii) refractory compounds formed by dibenzothiophene (DBT) and its alkyl homologues ($M_x$DBT). Reactive compounds are the most abundant species accounting for 6603 ppm of elementary sulfur. On the other hand, benzothiazole (BTZ), not present in LCO, is the most abundant sulfur compound in STO (accounting for 3663 ppm of total sulfur), and comes from the sulfur added in the vulcanization process to modify the polymeric structure of the rubber in order to obtain cross-linked structures to enhance mechanical properties, resistance and durability of the tires [56]. Furthermore, dibenzothiophene type structures can be also found in STO, being $M_2$DBT and $M_3$DBT the most abundant groups with 3341 and 3294 ppm, respectively. As it was expected, a whole distribution of the sulfur species can be found in STO/LCO blend, being the reactive species the most abundant accounting for 6015 ppm. Even though, the amount of refractory species in the STO/LCO blend is higher than that of the LCO, so its hydrodesulfurization will be more challenging. The results of the APPI FT-ICR MS of the LCO and STO feeds (presented in Figure S1, Supporting Information) reveal that the most predominant sulfur species in both samples are alkylated benzothiophenes (DBE = 6) and alkylated dibenzothiophenes
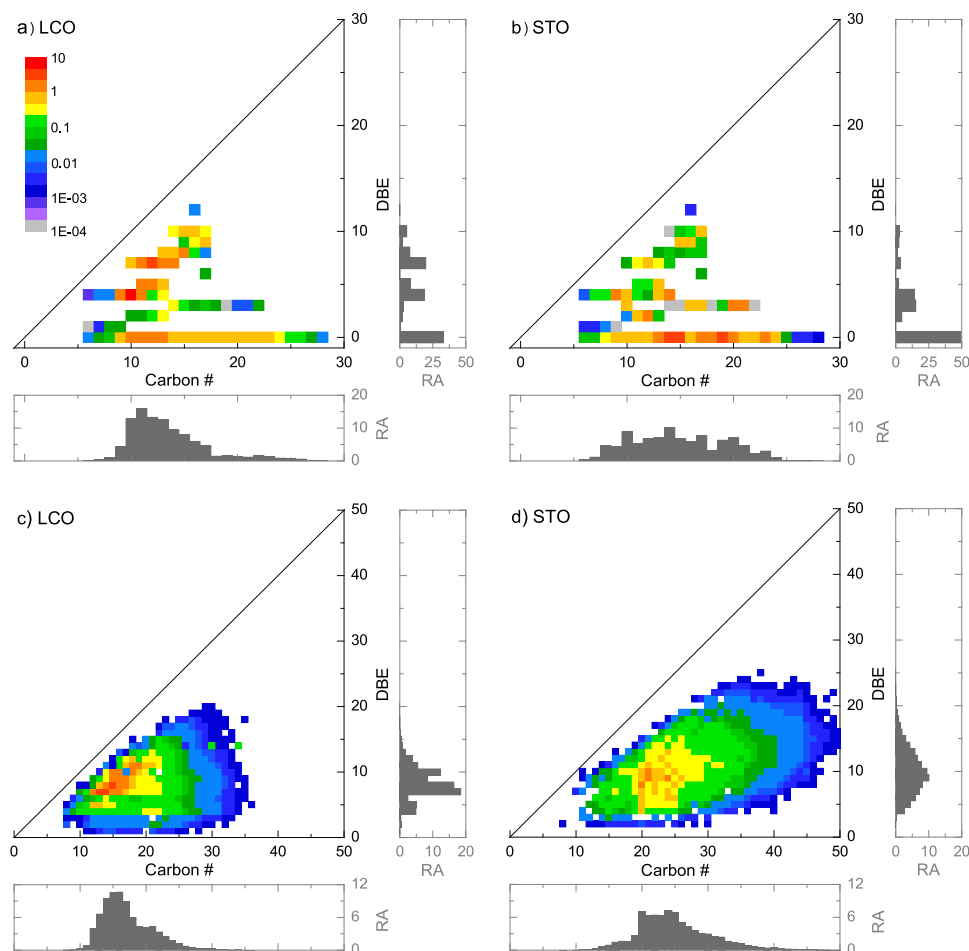
**Fig. 3.** Composition of LCO and STO measured by means of comprehensive gas chromatography a–b) and of APPI FT-ICR MS cd) according to CH species. The scale bar represents relative abundance (RA) for the color-coded DBE vs carbon number (C#) plots.

(DBE = 9). On the other hand, STO sulfur species are heavier and lay in a broader distribution compared to these of the LCO.

According to the compositional similarities, STO has the proper composition to be blended with the LCO prior the hydrotreatment of the latter. The results of the composition of the STO/LCO blend will be displayed below together with the products of hydrotreating for better comparing the performance of the catalysts.

### 3.3. Hydrocracking and hydrodearomatization

To assess the extent of hydrocracking (HC) and hydrodearomatization (HDA) reactions occurring in hydroprocessing, both FID GC × GC and APPI FT-ICR MS techniques can give essential information. In the DBE vs. C# graph, the relative abundance changes downwards or leftwards correspond to hydrogenation (lowering DBE) or hydrocracking (lowering C#), respectively [57]. The results of the analysis of the reactant (STO/LCO blend) and products from its hydroprocessing using CoMo/ALM, NiMo/ASA or NiW/USY catalysts at 400 °C are displayed in Figs. 4 and 5. The results of FID GC × GC (Fig. 4) indicate that the STO/LCO blend assembles qualitatively the same species analyzed in the individual components (Fig. 3a, b) and quantitatively by combining the amount of species corresponding to 80% of LCO and 20% of STO. The STO/LCO blend contains significant amount of species with DBE = 4, 7 and 10, and C# = 15+ species (with a maximum in

C# = 11). More specifically, significant amounts of tetramethyl benzene (C# = 10, DBE = 4) and dimethyl naphthalene (C# = 12, DBE = 7) have been detected in the blend. The hydroprocessing products are very similar regardless the use of CoMo/ALM, NiMo/ASA or NiW/USY catalysts. In the products, several fractions have converted, such as the ones with DBE = 7, 10 and C# = 15+, into lighter and more hydrogenated products, such as the ones with DBE = 5 and C# = 15+. In fact, we observe a concentration increase of 1-ring aromatics (DBE = 4) and paraffins (DBE = 0) from values of 27 to ca. 38 wt% and of 28 to ca. 44 wt%, respectively. More specifically, significant amounts of polyalkyl benzenes or dimethyl tetralin (C# = 12, DBE = 5), and paraffins with C# = 11–12. Thus, a sequenced hydrogenation of aromatic rings (dimethyl naphthalene → dimethyl tetralin) and ring opening of naphthenic rings (dimethyl tetralin → polyalkyl benzenes or $C_{12}$ paraffins occur. Being the extent of this sequence relatively similar for each catalyst employed. NiW/USY catalyst shows slightly better hydrogenation performance mainly caused by its higher metallic loading (Table 1) and the higher surface exposure (Fig. 1a). Moreover, the higher and stronger acidity of NiW/USY catalyst should be responsible of enhanced ring opening reactions, facilitating the initial hydrogenation reactions by avoiding the possible thermodynamic control of these reactions.

In terms of hydrocracking, STO/LCO blend has a wide carbon distribution with a maximum in C# = 11–12, while for the products a
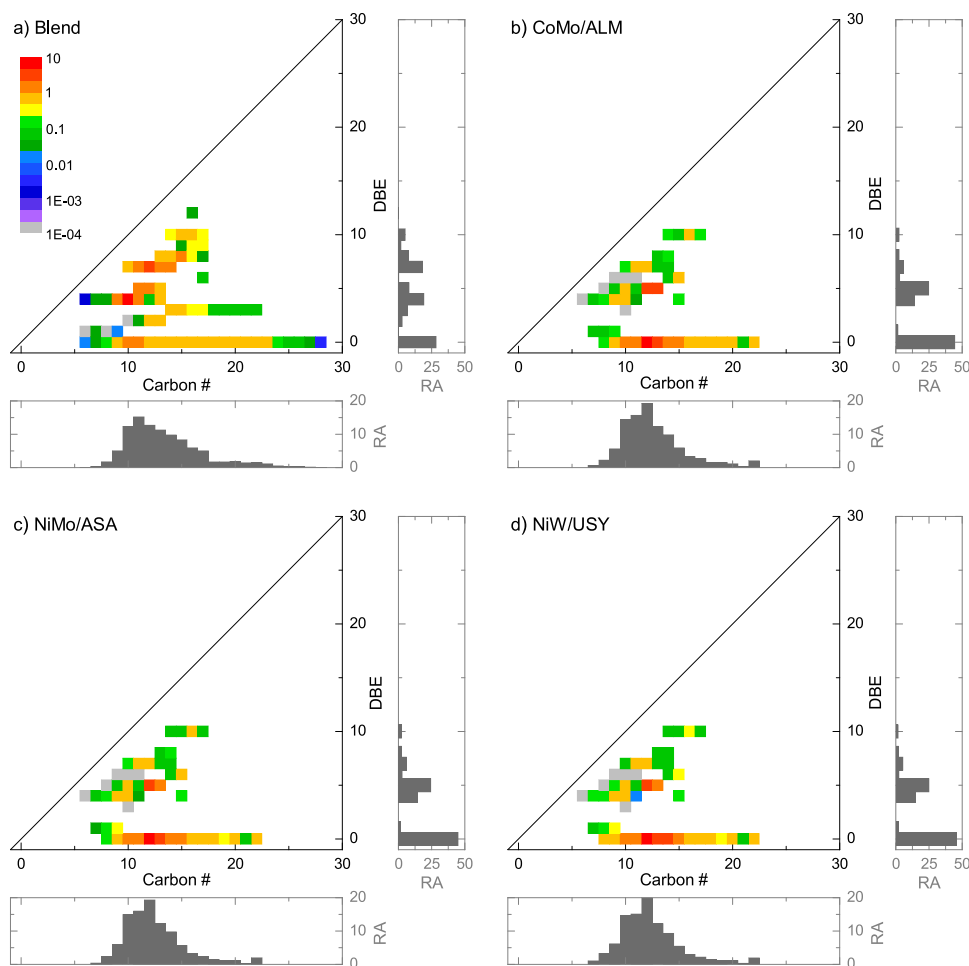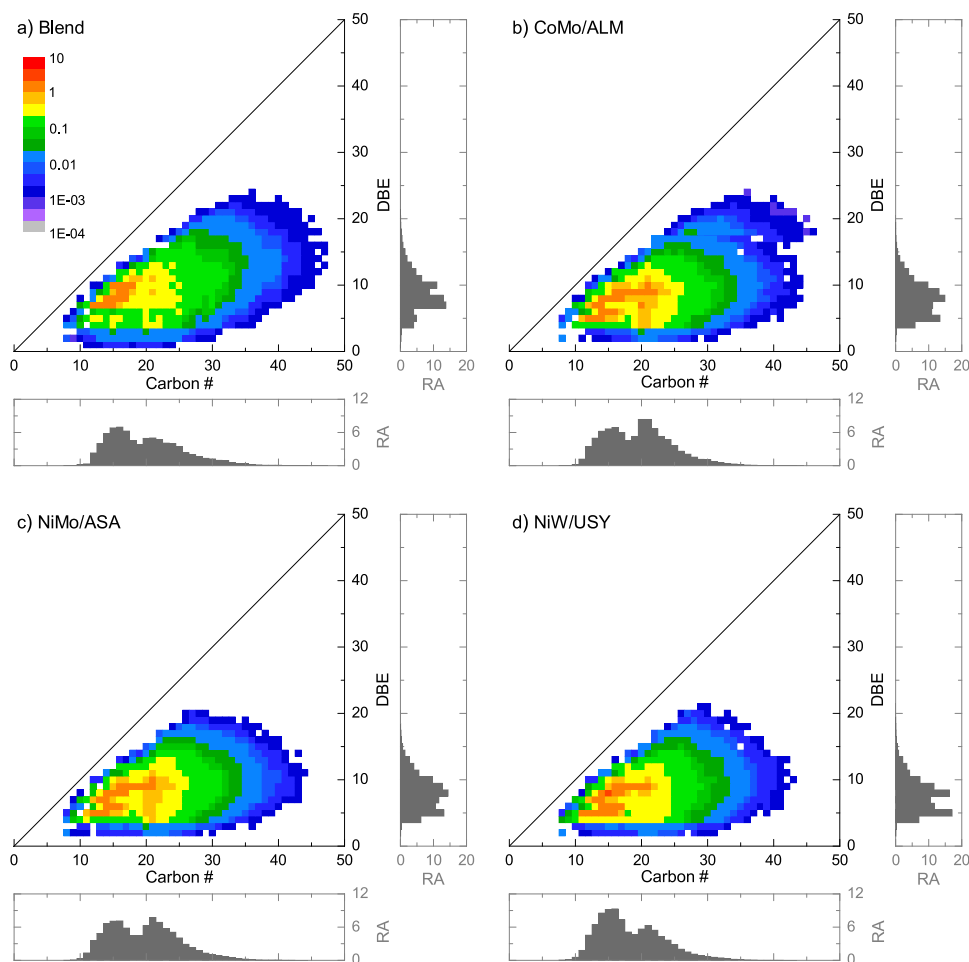
**Fig. 4.** Color-coded abundance plots of DBE versus carbon number for CH species in the feedstock a) and obtained products b–d). Results obtained by means of FID GC × GC. The scale bar represents relative abundance (RA) within the compound class.

narrower distribution is obtained with a maximum shifted towards C# = 12–13. The carbon number distribution indicates that the heavier $C_{15+}$ fraction from the blend and more specifically from the STO has been hydrocracked into lighter diesel fraction ($C_{11-12}$). In addition, the degree of hydrocracking is relatively similar for all catalysts used. NiMo/ASA and NiW/USY show somewhat better hydrocracking performance as consequence of their higher total acidity and acidic strength (Fig. 1b). Besides, ring opening reactions can be circumscribed to hydrocracking, do not decrease the number of carbons but have a very positive effect on accelerating hydrogenation reactions and improve the quality of products (gasoline and diesel) [45,58,59]. As previously mentioned, these ring opening reactions are faster over NiW/USY catalyst.

The distributions of CH species for the blend and products obtained by means of APPI FT-ICR MS are shown in Fig. 5. As it happened for the individual components, the number and distribution of species obtained for the blend (Fig. 5a) by this technique is different than that obtained by FID GC × GC (Fig. 4). APPI FT-ICR MS shows that the feed contains species with C# up to ~45 and DBE up to 25. The molecular distribution in terms of carbon number shows a bimodal distribution or two clusters of species with maxima at C# = 16 and 20–21. The first one is strongly linked with LCO and the second one has a greater contribution of STO.

The most abundant species in the blend correspond to highly alkylated 2-ring aromatics (DBE = 7), followed by highly alkylated 3 and 1-ring aromatics (DBE = 10 and 4, respectively). In terms of the products of CoMo/ALM catalyst (Fig. 5b), the first cluster of species (at C# = 16) remains unaffected whereas the second one (at 20–21) increases due to the hydrocracking of heavier $C_{25+}$ species. At the same time, highly alkylated 3- and 2-ring aromatics are hydrogenated to highly alkylated 1-ring aromatics. The products obtained with the NiMo/ASA catalyst are similar in composition (Fig. 5c) to these of CoMo/ALM catalyst, so that their hydrocracking and hydrodearomatization activities are similar. On the other hand, NiW/USY catalyst (Fig. 5d) yields (i) greater fraction of lighter species (around C# = 16), (ii) more concentration of species in the cluster around C# = 20–21, while (iii) lower fraction of the heaviest $C_{25+}$ species. In fact, this catalyst is particularly efficient for hydrogenating highly alkylated 3-ring aromatics (DBE = 10). As observed in the results of FID GC × GC (Fig. 4), NiW/USY catalyst has the fastest rates of hydrocracking and hydrogenation due to its higher total acidity and acidic strength (Fig. 1b). However, these rates are not enough to promote an aromatic over saturation. This effect is accompanied with a low utilization of hydrogen and considerable yield of light paraffins with a lower value [60].

**Fig. 5.** Color-coded abundance plots of DBE versus carbon number for CH species in the feedstock a) and obtained products b–d). Results obtained by means of APPI FT-ICR MS. The scale bar represents relative abundance (RA) within the compound class.

**Table 3**
Sulfur speciation of reaction products in the hydroprocessing of the STO/LCO blend.

|  | STO/LCO | CoMo/ALM | NiMo/ASA | NiW/USY |
|---|---|---|---|---|
| DBT (ppm) | 259 | – | – | – |
| $M_1$ DBT (ppm) | 1020 | 23 | 35 | 92 |
| $M_2$ DBT(ppm) | 1672 | 88 | 168 | 111 |
| $M_3$ DBT (ppm) | 1444 | 80 | 122 | 41 |
| Sulfur (ppm) | 10,410 | 214 | 325 | 222 |

### 3.4. Hydrodesulfurization

One of main goal of hydroprocessing is to remove the content of heteroatoms, especially sulfur, from the feedstock. Table 3 summarizes the sulfur and sulfur species concentrations of the feed and products as obtained by PFPD GC analysis. These concentrations could be anticipated by the concentration of the individual components of the blend shown in Table 2. Besides, Table 3 also displays the sulfur and sulfur species concentrations of the products. The STO/LCO blend has a total sulfur content of 10410 ppm with 3116 ppm of alkylated DBTs ($M_2$ and $M_3$DBT). In the products, the sulfur content drops to 325–214 ppm with conversion higher than 97%. CoMo/ALM catalyst is the most effective towards reducing the total sulfur concentration while NiW/USY catalyst is the most efficient to decrease alkylated DBTs. These species are the most refractory among sulfur ones, especially if their substituents are located in 4 and 6 positions [61,62,75]. All catalysts remove completely species such as benzothiazole (only present in the STO, 3663 ppm,

Table 2), benzothiophene and its alkyl derivatives.

Additionally, sulfur containing compounds (the $S_1$ class) have been characterized by APPI FT-ICR MS. The results are shown in Fig. 6. In the blend (Fig. 6a), the $S_1$ species are distributed along a wide range of DBEs (2–19) and C# (8–40), but the most abundant species correspond to highly alkylated benzothiophenes (BTs, DBE = 6) and lowly alkylated dibenzothiophenes (DBTs, DBE = 9), particularly 4,6-$M_2$DBT (C# = 14 and DBE = 9). Benzothiazole (C# = 7, DBE = 6) has being detected in the STO/LCO blend using APPI FT-ICR MS but within the $S_1N_1$ class. The projection of the distribution of carbon number shows a bimodal distribution with their maxima centered at C# = 14 and 19. The overall abundance of $S_1$ species considerably decreases with all the hydrotreating catalysts in the following order CoMo/ALM < NiW/USY < NiMo/ASA. Note that the scale of the projections between the feed and the products has decreased almost one order of magnitude. Sulfur molecules with more than C# = 26 and less than C# = 10 have been totally removed with all the catalysts, at the same time the removal of alkylated BTs is very efficient in particular with the CoMo/ALM catalyst. In terms of carbon distribution, NiMo/ASA catalyst has a homogeneous HDS activity along the carbon number, whereas CoMo/ALM and particularly NiW/USY catalysts are more selective towards the removal of the heavier $C_{20+}$ sulfur fraction. The differences in the sulfur speciation results provided by PFPD GC and APPI FT-ICR MS are attributed to the fact that each technique is more sensitive to analyze the lighter $C_{12-}$ or heavier $C_{12+}$ fractions, respectively. The results of PFPD GC and APPI FT-ICR MS confirm that the reactivity and disappearance of DBT species is the rate determining step among the HDS pathways with all the catalyst employed.
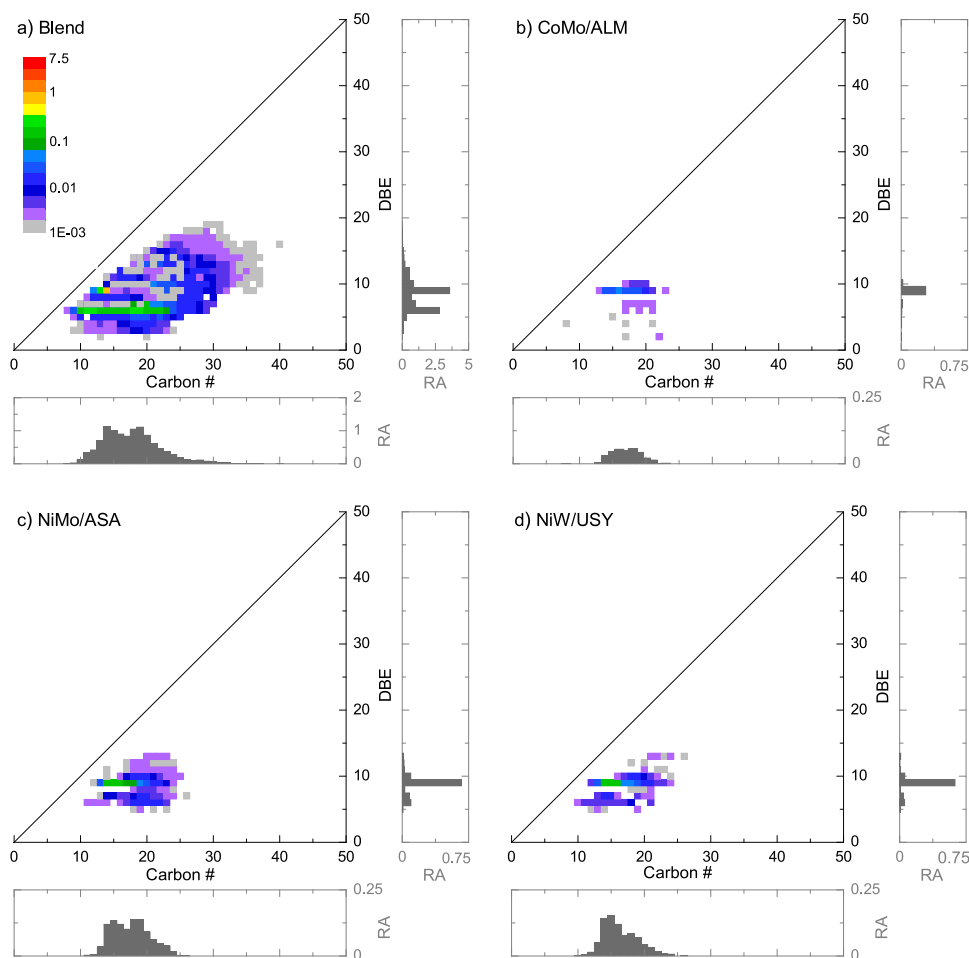
**Fig. 6.** Color-coded abundance plots of DBE versus carbon number for $S_1$ species in the feedstock a) and obtained products b–d). Results obtained by means of APPI FT-ICR MS. The scale bar represents relative abundance (RA) within the compound class.

The enhanced HDS activity of CoMo/ALM catalyst over the rest is due to a number of intrinsic advantages: (i) broader pores of 10.8 nm (Fig. 1a), which improves the accessibility of the bulkiest sulfur molecules from STO; (ii) highest total acidity (0.542 $mmol_{t-BA}$ $g^{-1}$, Fig. 1b), which is crucial for HDS [6]; (iii) greater metallic edge accessibility (Fig. 2d) and optimal Co/Mo ratio (0.23, Table 1) for boosting hydrogenolysis reactions instead of hydrogenation ones [63]. Furthermore, considering the higher sulfur removal (Fig. 6b) and the moderate aromatics removal (Fig. 5b) obtained, it can be concluded that CoMo/ALM catalyst promotes the direct desulfurization over the indirect pathway of hydrogenation and desulfurization [64].

### 3.5. Hydrodenitrogenation

Nitrogen species present in both STO and LCO (Table 2) can be divided into two groups: (i) basic species, that adsorb on the acidic sites of the catalyst; and (ii) nonbasic species, that adsorb on the metal sulfide active sites of the catalyst [65]. Consequently, the fact that N species inhibit HDS reactions makes their removal a prior target in hydroprocessing [17]. Fig. 7 shows the DBE vs. carbon number distribution of $N_1$ species assigned from positive-ion ESI FT-ICR mass spectra. ESI instead of APPI was used as it is more sensitive toward

nitrogen compounds (does not efficiently ionize CH species). The STO/LCO blend has nitrogen species distributed along a wide range of species (C# = 6–43; DBE = 0–23), with maxima at C# = 15–18 and DBE = 9–13. These species correspond to alkylated indoles, carbazoles, benzocarbazoles, quinolines and acridines with diverse degree of aromatic condensation (corresponding DBEs are 6, 9, 12, 7 and 10, respectively). The hydrotreated products using the three catalysts show an efficient removal of the heaviest and more condensed $C_{25+}$ nitrogen fraction, with a significant increase of lighter fraction with C# = 14–16 and DBE = 4–9, corresponding to lighter and less aromatic carbazoles, indoles and quinolines [66]. Together with the overall decrease of abundance of nitrogen species, a parallel shift in the profiles of DBE and carbon number occur, so that nitrogen species suffer parallel HDN, HDA and HC reactions. These parallel reactions, not observed for sulfur species and HDS performance (Fig. 6), are linked to the intrinsic HDN mechanisms on transition metal based catalysts, which requires the prior aromatic ring hydrogenation and probable ring opening reactions [35,37,67].

The HDN performance of the NiW/USY catalyst stood out, which can be correlated to the following advantages: (i) acid sites with greater strength (550 J $mmol_{t-BA}^{-1}$) and higher proportion of BAS/LAS (2.39), as shown in Fig. 1b, which improves the adsorption and reaction of basic
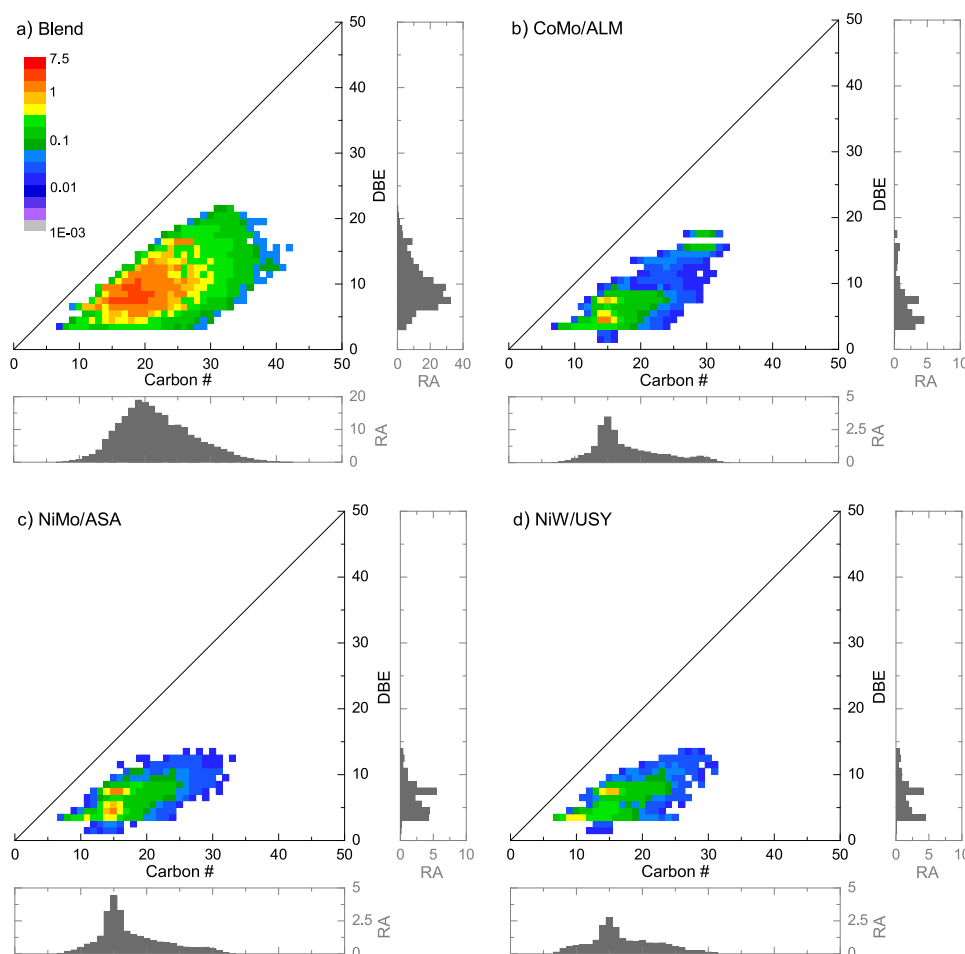
**Fig. 7.** Color-coded abundance plots of DBE versus carbon number for $N_1$ species in the feedstock a) and obtained products b–d). Results obtained by means of ESI FT-ICR MS. The scale bar represents relative abundance (RA) within the compound class.

nitrogen compounds [68]; and (ii) high loading (Table 1) of highly stacked $WS_2$ crystals (Fig. 2f). At the same time, the greater HDN activity of NiW/USY catalyst can be ascribed to the faster rates of parallel HDA and HC of nitrogen species, which ultimately make nitrogen more accessible to the reaction.

### 3.6. Hydrodeoxygenation

The oxygen content of the conventional petroleum derived stocks is less than 2 wt%, with an average value of 0.5 wt% [69] and reaching values up to 8 wt% for asphaltenes and resins. The mainstream in hydrodeoxygenation (HDO) deals with the conversion of biomass-derived stocks instead of the petroleum derived ones [20,70]. Fig. 8 shows the DBE vs. C# distributions of $O_1$ species assigned from APPI FT-ICR mass spectra. Among the main heteroatomic species, $O_1$ is the less abundant class according to the total relative summation of abundances. The oxygen containing species in the STO/LCO blend cover a wide range of species (C# = 10–35; DBE = 5–18) with a maximum at C# = 20 and DBE = 20. These species are alkylated furans with several degrees of aromatic condensation, in particular alkylated dibenzofurans (DBE = 9). The hydrotreated products using the three catalysts have suffered a selective HDO of alkylated naphthobenzofuranes with certain degree of formation of hydrogenated oxygen species with DBE ≈ 4–5 and hydrocracked oxygen species with C# = 8, 14 and 17. These observations lead to conclude that during HDO, oxygenated species suffer parallel HDA and HC which makes oxygen moieties more accessible to the metallic sites of the catalysts. The abundance of dibenzofurans remains almost unchanged between the blend and all the catalysts,

proving that dibenzofurans are relatively unreactive.

In the conditions studied, the better HDO performance is obtained with the NiMo/ASA catalyst. Given the fact that the surface, metallic and acidic properties of this particular catalyst (Fig. 1) are intermediate between the three, a higher performance should be attributed to the particular behavior of the metallic phase (Ni and Mo) over the rest of the phases, as proved before [71]. Additional routes are dehydration catalyzed by acid sites, and decarboxylation-decarbonylation catalyzed by the metallic phases, particularly Ni [72]. Even though quite good results were also obtained with NiW/USY catalyst, NiW catalysts requires much higher metallic exposure than NiMo catalyst in order to have comparable activity [73].

### 4. Discussion

Screening and comparing the performance of hydrotreating catalysts to upgrade the STO/LCO blend is difficult due to the multiplicity of reactions involved in the process. In order to facilitate this discrimination, we have defined a number of conversions as listed in Table 4. Each conversion ($X_i$) is assigned to the disappearance of a fraction/abundance ($C_i$) of the total species analyzed, and thus normalized, by each technique indicated in Table 4 too. Then each conversion has been calculated as follows:

$$X_i = \frac{C_i\ |_{feed} - C_i\ |_{products}}{C_i\ |_{feed}} \tag{2}$$

The conversions defined in Table 4 have been represented for the three catalysts in Fig. 9. Fig. 9a shows the HC and HDA performance of
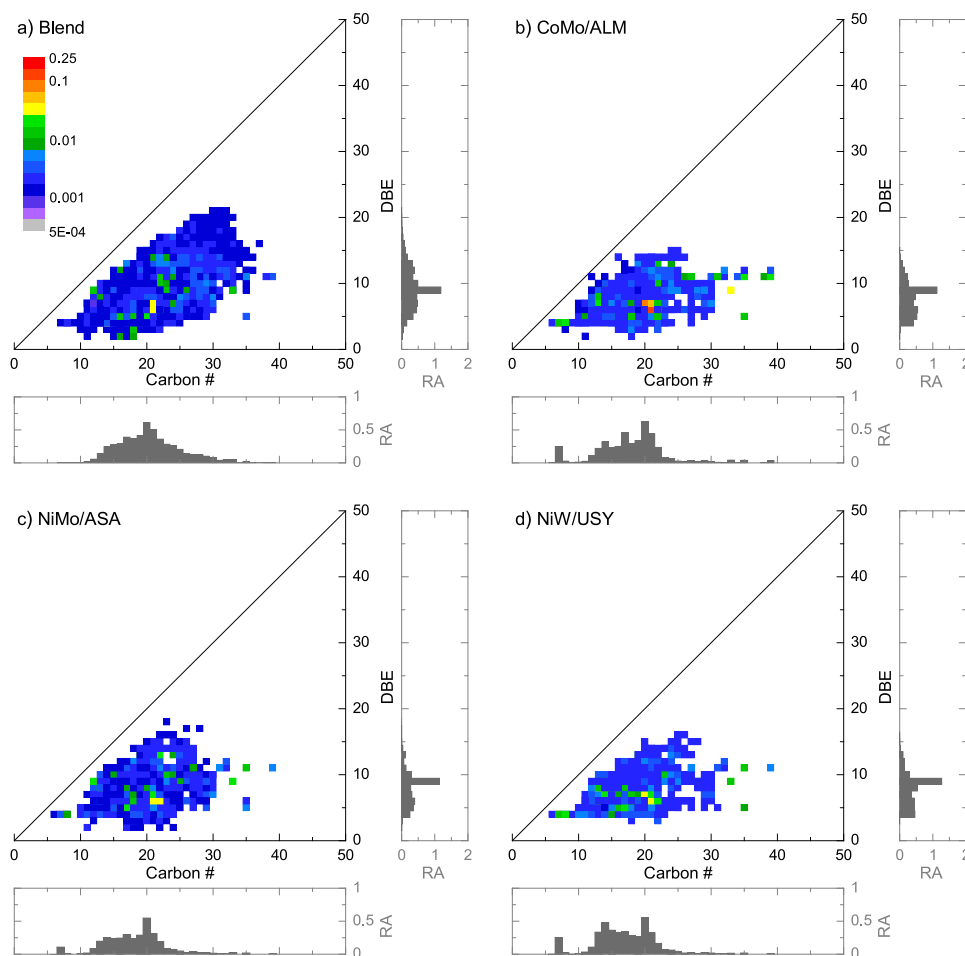
**Fig. 8.** Color-coded abundance plots of DBE versus carbon number for $O_1$ species in the feedstock a) and obtained products b–d). Results obtained by means of APPI FT-ICR MS. The scale bar represents relative abundance (RA) within the compound class.

the catalysts. NiW/USY catalyst has the best HC and HDA performances particularly in the conversion of high boiling point hydrocarbons (BP380 + SD and BP420 + SD), species with more than C# = 20 and 30 (C20 + CH and C30 + CH, respectively) and highly condensed aromatic species (D7 + CH and D9 + CH). CoMo/ALM and NiMo/ASA catalyst share similar HC and HDA activities, but lower than these of NiW/USY catalyst. CoMo/ALM shows greater conversion of high boiling point hydrocarbons (BP420 + SD) compared with NiMo/ASA which can only be linked with a greater C-C hydrogenolysis performance of CoMo against NiMo [74], and the higher number of acid sites (Fig. 1b). Note that the rest of acid properties of NiMo/ALM catalyst have greater values than these of the CoMo/ALM catalyst (Fig. 1b).

In terms of HDS activity, Fig. 9b shows the values of S species removal using different techniques. All values are higher than 0.8 so that the scale of this graph has changed between 0.8–1.0. CoMo/ALM catalyst shows a greater HDS activity in terms of the removal of total sulfur (TS and TPFPD), heavy S species (C20 + S), alkylated benzothiophene (D6) and alkylated dibenzothiophenes (D9S, D9PFPD and D9C14PFPD). The following catalyst in terms of HDS activity (by means of all conversions defined before) is NiW/USY catalyst, and then NiMo/ASA catalyst.

In terms of HDN and HDO activity, Fig. 9c-d shows the values of N and O species removal using different techniques. For HDN performance, all values are higher than 0.8 so that the scale of this graph has changed between 0.8–1.0. NiW/USY catalyst displays the highest HDN activity in terms of removing total nitrogen (TN), and heavy N species

(C20 + N and C30 + N). CoMo/ALM catalyst has lower HDN activity in terms of the direct denitrification reaction but higher indirect hydrogenation and, thus, displays higher hydrogenation of highly condensed aromatics with N (D8.5 N, D10.5 N and D12.5 N). Interestingly, in terms of HDO performance NiMo/ASA catalyst displays the greatest activity, with higher conversions of total oxygenates (TO), heavy O species (C20 + O and C30 + O), alkylated dibenzofurans (D9O) and highly condensed aromatics with O (D10 + O). So, it can be concluded that NiW/USY catalyst shows a better overall performance.

Unfortunately, there is not a single technique that is able to fulfill the broad chemical composition of the feed and the products accurately. FID GC × GC is very reliable in terms of the concentration of light fractions and aliphatics (paraffins, and naphthenes). On the other hand, APPI/ESI FT-ICR MS is very reliable in terms of the detection of heavy hydrocarbons and aromatics. Simulated distillation can get a complete picture of the analyte, but the information obtained is rather limited.

The results shown in this work indicate that the overall mechanisms of HDS, HDN, HDA, HDO and HC are the same for all the catalysts studied. The final catalytic performance materialized in the indexes of Table 4 and Fig. 9 cannot be directly linked with any particular feature of the catalyst but a combination of factors including the reaction media composition. However, the methodology to quantify the catalytic performance developed in this work can be used to get a more precise picture of the "activity", in order to make structure-activity correlations in the future.

**Table 4**
Definitions of conversions assigned to establish the catalysts screening.

| Conversion | Technique | $C_i$ |
|---|---|---|
| *Hydrocracking* (HC) | | |
| BP380 + SD | SD | Fraction with a boiling point higher than 380 °C |
| BP420 + SD | SD | Fraction with a boiling point higher than 420 °C |
| C20 + FID | FID GC × GC | Fraction of species with more than 20 carbons |
| C20 + CH | APPI FT-ICR MS | Abundance of CH species with more than 30 carbons |
| C30 + CH | APPI FT-ICR MS | Abundance of CH species with more than 30 carbons |
| *Hydrodearomatization* (HDA) | | |
| D7 + FID | FID GC × GC | Fraction of species with DBE > 7 (2-rings aromatics) |
| D9 + FID | FID GC × GC | Fraction of species with DBE > 9 |
| D7 + CH | APPI FT-ICR MS | Abundance of CH species with DBE > 7 (2-rings aromatics) |
| D9 + CH | APPI FT-ICR MS | Abundance of CH species with DBE > 9 |
| *Hydrodesulfurization* (HDS) | | |
| TS | APPI FT-ICR MS | Abundance of S species |
| C20 + S | APPI FT-ICR MS | Abundance of S species with more than 20 carbons |
| D6S | APPI FT-ICR MS | Abundance of S species with DBE = 6 (alkylated BTs) |
| D9S | APPI FT-ICR MS | Abundance of S species with DBE = 9 (alkylated DBTs) |
| TPFPD | PFPD GC | Fraction of S species |
| D9PFPD | PFPD GC | Fraction of S species with DBE = 9 (alkylated DBTs) |
| D9C14PFPD | PFPD GC | Fraction of $M_2DBT$ |
| *Hydrodenitrification* (HDN) | | |
| TN | ESI FT-ICR MS | Abundance of N species |
| C20 + N | ESI FT-ICR MS | Abundance of N species with more than 20 carbons |
| C30 + N | ESI FT-ICR MS | Abundance of N species with more than 30 carbons |
| D8.5 N | ESI FT-ICR MS | Abundance of N species with DBE = 8.5 (protonated) |
| D10.5 N | ESI FT-ICR MS | Abundance of N species with DBE = 10.5 (protonated) |
| D12.5 N | ESI FT-ICR MS | Abundance of N species with DBE = 12.5 (protonated) |
| *Hydrodeoxygenation* (HDO) | | |
| TO | APPI FT-ICR MS | Abundance of O species |
| C20 + O | APPI FT-ICR MS | Abundance of O species with more than 20 carbons |
| C30 + O | APPI FT-ICR MS | Abundance of O species with more than 30 carbons |
| D9O | APPI FT-ICR MS | Abundance of O species with DBE = 9 (alkylated dibenzofurans) |
| D10 + O | APPI FT-ICR MS | Abundance of O species with DBE > 10 |
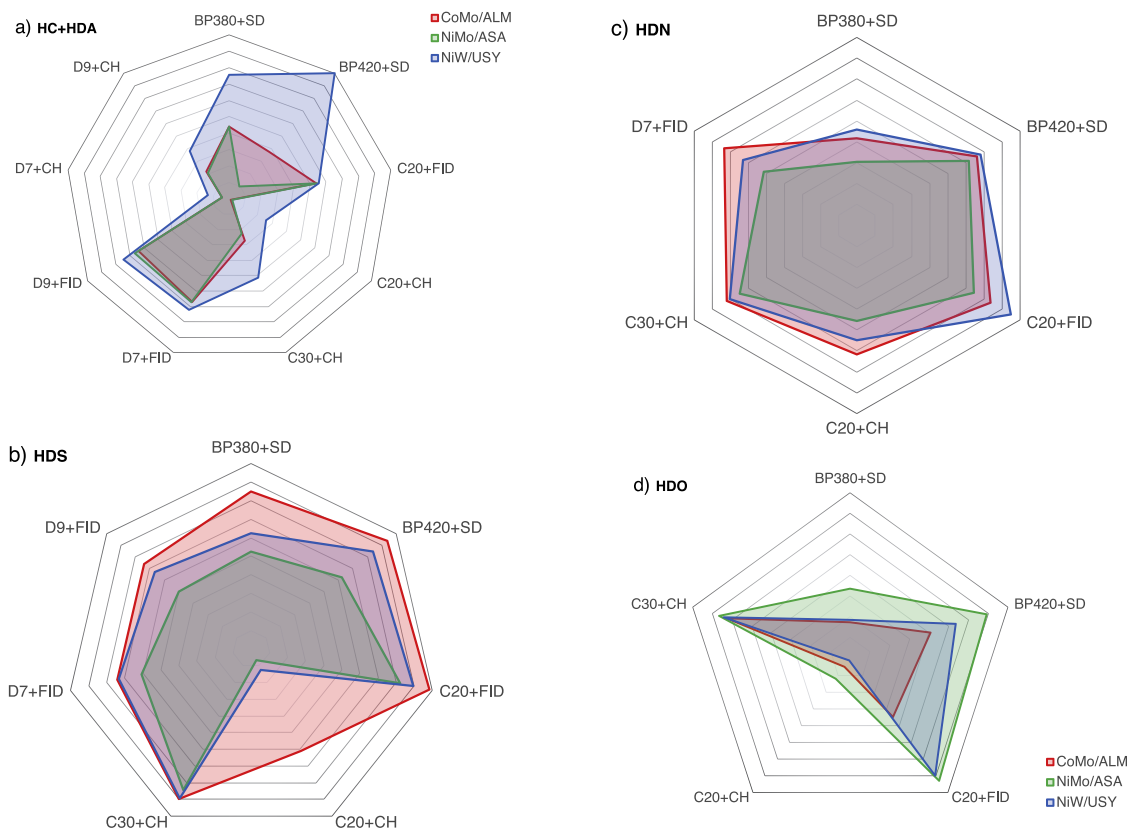


**Fig. 9.** Conversions reached for the different goals with all the studied catalysts: a) HC and HDA performance, b) HDS performance, c) HDN performance and d) HDO performance. For HDS and HDN performances, all values are higher than 0.8 so that the scale of this graph has changed between 0.8–1.0.

## 5. Conclusions

In this work, we have tested three industrial catalysts (CoMo/Al$_2$O$_3$, NiMo/SiO$_2$-Al$_2$O$_3$ and NiW/USY zeolite) in the hydroprocessing of a blend of scrap tire oil (STO, 20 vol%) and light cycle oil (LCO). Using industrially relevant hydroprocessing conditions, these catalysts perform relatively similar among them, producing high-quality fuels with significantly less concentration of contaminants such as sulfur, nitrogen or oxygen. Taking the different features of the catalysts in terms of metallic and acidic sites, the similar performance is due to the rate controlling effect of the heaviest molecules of the feed, particularly present in the STO.

Combining the results of FID-MS GC × GC and APPI/ESI FT-ICR MS, which are complementary techniques, we can obtain a faithful picture of the composition of the feed and products, getting insights into individual and collective conversions of species within the main reaction pathways: hydrodesulfurization, hydrodenitrogenation, hydrodeoxygenation, hydrodearomatization and hydrocracking.

Strengthening the quantitative effort is important to asses a catalytic performance comparison, which lead to conclude the following: (i) CoMo/Al$_2$O$_3$ catalyst has shown the highest hydrodesulfurization rate as a consequence of its superior exposure of the metal, its higher total acidity and higher average pore size, altogether boosting the direct desulfurization reactions; (ii) NiMo/SiO$_2$-Al$_2$O$_3$ catalyst shows a good performance in hydrocracking and hydrodearomatization, but it excels in hydrodeoxygenation due to its higher dispersion and concentration of Brønsted acidic sites (promoting also decarbonylation and decarboxylation reactions); and (iii) NiW/USY catalyst has shown very interesting results in hydrodenitrogenation, hydrocracking and hydrodearomatization, especially in the removal of polyaromatics, as a consequence of its superior acidic properties.

This work galvanizes the need of combining different analytical techniques to assess the composition of complex feed and products in catalytic processing and treat the results quantitatively in order to faithfully understand the kinetics and catalytic behavior.

## Acknowledgments

## Appendix A. Supplementary data

Supplementary material related to this article can be found, in the online version, at doi:https://doi.org/10.1016/j.apcatb.2019.117863.

## References

[1] R. Palos, A. Gutiérrez, J.M. Arandes, J. Bilbao, Catalyst used in fluid catalytic cracking (FCC) unit as a support of NiMoP catalyst for light cycle oil hydroprocessing, Fuel 216 (2018) 142–152.

[2] G. Escalona, A. Rai, P. Betancourt, A.K. Sinha, Selective poly-aromatics saturation and ring opening during hydroprocessing of light cycle oil over sulfided Ni-Mo/SiO$_2$-Al$_2$O$_3$ catalyst, Fuel 219 (2018) 270–278.

[3] Y. Ghrib, N. Frini-Srasra, E. Srasra, J. Martínez-Triguero, A. Corma, Synthesis of cocrystallized USY/ZSM-5 zeolites from kaolin and its use as fluid catalytic cracking catalysts, Catal. Sci. Technol. 8 (2018) 716–725.

[4] A. Ibarra, E. Rodríguez, U. Sedran, J.M. Arandes, J. Bilbao, Synergy in the cracking of a blend of bio-oil and vacuum gasoil under fluid catalytic cracking conditions,

[5] Ind. Eng. Chem. Res. 55 (2016) 1872–1880.

[5] B. Kunwar, S.D. Deilami, L.E. Macaskie, J. Wood, P. Biller, B.K. Sharma, Nanoparticles of Pd supported on bacterial biomass for hydroprocessing crude bio-oil, Fuel 209 (2017) 449–456.

[6] I. Hita, A. Gutiérrez, M. Olazar, J. Bilbao, J.M. Arandes, P. Castaño, Upgrading model compounds and Scrap tires Pyrolysis Oil (STPO) on hydrotreating NiMo catalysts with tailored supports, Fuel 145 (2015) 158–169.

[7] R. Palos, A. Gutiérrez, J.M. Arandes, J. Bilbao, Upgrading of high-density polyethylene and light cycle oil mixtures to fuels via hydroprocessing, Catal. Today 305 (2018) 212–219.

[8] I. Hita, M. Arabiourrutia, M. Olazar, J. Bilbao, J.M. Arandes, P. Castaño, Opportunities and barriers for producing high quality fuels from the pyrolysis of scrap tires, Renewable Sustainable Energy Rev. 56 (2016) 745–759.

[9] G. López, M. Olazar, R. Aguado, J. Bilbao, Continuous pyrolysis of waste tyres in a conical spouted bed reactor, Fuel 89 (2010) 1946–1952.

[10] J.D. Martínez, M. Lapuerta, R. García-Contreras, R. Murillo, T. García, Fuel properties of tire pyrolysis liquid and its blends with diesel fuel, Energy Fuels 27 (2013) 3296–3305.

[11] G.C. Laredo, P.M. Vega Merino, P.S. Hernández, Light cycle oil upgrading to high quality fuels and petrochemicals: a review, Ind. Eng. Chem. Res. 57 (2018) 7315–7321.

[12] G. Fogassy, N. Thegarid, G. Toussaint, A.C. van Veen, Y. Schuurman, C. Mirodatos, Biomass derived feedstock co-processing with vacuum gas oil for second-generation fuel production in FCC units, Appl. Catal. B Environ. 96 (2010) 476–485.

[13] M. Marafi, E. Furimsky, Hydroprocessing catalysts containing noble metals: deactivation, regeneration, metals reclamation, and environment and safety, Energy Fuels 31 (2017) 5711–5750.

[14] P. Rayo, A. Rodríguez-Hernández, P. Torres-Mancera, J.A.D. Muñoz, J. Ancheyta, R. García de León, Different alumina precursors in the preparation of supports for HDT and HDC of Maya crude oil, Catal. Today 305 (2018) 2–12.

[15] C. Song, An overview of new approaches to deep desulfurization for ultra-clean gasoline, diesel fuel and jet fuel, Catal. Today 86 (2003) 211–263.

[16] I.V. Babich, J.A. Moulijn, Science and technology of novel processes for deep desulfurization of oil refinery streams: a review, Fuel. 82 (2003) 607–631.

[17] K. Guo, Y. Ding, Z. Yu, One-step synthesis of ultrafine MoNiS and MoCoS monolayers as high-performance catalysts for hydrodesulfurization and hydrodenitrogenation, Appl. Catal. B Environ. 239 (2018) 433–440.

[18] F. Wang, J. Jiang, K. Wang, Q. Zhai, F. Long, P. Liu, J. Feng, H. Xia, J. Ye, J. Li, J. Xu, Hydrotreatment of lipid model for diesel-like alkane using nitrogen-doped mesoporous carbon-supported molybdenum carbide, Appl. Catal. B Environ. 242 (2019) 150–160.

[19] T. Cordero-Lanzac, R. Palos, I. Hita, J.M. Arandes, J. Rodríguez-Mirasol, T. Cordero, J. Bilbao, P. Castaño, Revealing the pathways of catalyst deactivation by coke during the hydrodeoxygenation of raw bio-oil, Appl. Catal. B Environ. 239 (2018) 513–524.

[20] T. Cordero-Lanzac, R. Palos, J.M. Arandes, P. Castaño, J. Rodríguez-Mirasol, T. Cordero, J. Bilbao, Stability of an acid activated carbon based bifunctional catalyst for the raw bio-oil hydrodeoxygenation, Appl. Catal. B Environ. 203 (2017) 389–399.

[21] Y. Gao, W. Han, X. Long, H. Nie, D. Li, Preparation of hydrodesulfurization catalysts using MoS$_3$ nanoparticles as a precursor, Appl. Catal. B Environ. 224 (2018) 330–340.

[22] Y. Sun, C. Yang, H. Shan, B. Shen, Characterization of the reaction performance for residue hydrotreating feedstocks, Energy Fuels 25 (2011) 269–272.

[23] J. Alvira, I. Hita, E. Rodríguez, J. Arandes, P. Castaño, A data-driven reaction network for the fluid catalytic cracking of waste feeds, Processes 6 (2018) 243.

[24] A.G. Marshall, C.L. Hendrickson, G.S. Jackson, Fourier transform ion cyclotron resonance mass spectrometry: a primer, Mass Spectrom. Rev. 17 (1998) 1–35.

[25] L.C. Krajewski, R.P. Rodgers, A.G. Marshall, 126 264 assigned chemical formulas from an atmospheric pressure photoionization 9.4 t fourier transform positive ion cyclotron resonance mass Spectrum, Anal. Chem. 89 (2017) 11318–11324.

[26] J.C. Putman, A.G. Marshall, Screening petroleum crude oils for ARN tetraprotic acids with molecularly imprinted polymers, Energy Fuels 30 (2016) 5651–5655.

[27] B.M. Ruddy, C.L. Hendrickson, R.P. Rodgers, A.G. Marshall, Positive ion electrospray ionization suppression in petroleum and complex mixtures, Energy Fuels 32 (2018) 2901–2907.

[28] W. Wang, M. Dong, C. Song, X. Cai, Y. Liu, Z. Liu, S. Tian, Structural information of asphaltenes derived from petroleum vacuum residue and its hydrotreated product obtained by FT-ICR mass spectrometry with narrow ion isolation windows, Fuel. 227 (2018) 111–117.

[29] T. Kekäläinen, T. Venäläinen, J. Jänis, Characterization of birch wood pyrolysis oils by ultrahigh-resolution fourier transform ion cyclotron resonance mass spectrometry: insights into thermochemical conversion, Energy Fuels 28 (2014) 4596–4602.

[30] I. Miettinen, M. Mäkinen, T. Vilppo, J. Jänis, Compositional characterization of phase-separated pine wood slow pyrolysis oil by negative-ion electrospray ionization fourier transform ion cyclotron resonance mass spectrometry, Energy Fuels 29 (2015) 1758–1765.

[31] I. Miettinen, S. Kuittinen, V. Paasikallio, M. Mäkinen, A. Pappinen, J. Jänis, Characterization of fast pyrolysis oil from short-rotation willow by high-resolution Fourier transform ion cyclotron resonance mass spectrometry, Fuel. 207 (2017) 189–197.

[32] Z. Li, J. Gao, G. Wang, Q. Shi, C. Xu, Influence of nonbasic nitrogen compounds and condensed aromatics on coker gas oil catalytic cracking and their characterization, Ind. Eng. Chem. Res. 50 (2011) 9415–9424.

[33] T. Liu, J. Lu, X. Zhao, Y. Zhou, Q. Wei, C. Xu, Y. Zhang, S. Ding, T. Zhang, X. Tao,

L. Ju, Q. Shi, Distribution of vanadium compounds in petroleum vacuum residuum and their transformations in hydrodemetallization, Energy Fuels 29 (2015) 2089–2096.

[34] M. Liu, L. Zhang, S. Zhao, D. Zhao, Transformation of nitrogen compounds through hydrotreatment of Saudi Arabia atmospheric residue and supercritical fluid extraction subfractions, Energy Fuels 30 (2016) 740–747.

[35] M. Liu, L.Z. Zhang, C. Zhang, S.H. Yuan, D.Z. Zhao, L.H. Duan, Transformation of nitrogen-containing compounds in atmospheric residue by hydrotreating, Korean J. Chem. Eng. 35 (2018) 375–382.

[36] C.M. Celis-Cornejo, D.J. Pérez-Martínez, J.A. Orrego-Ruiz, V.G. Baldovino-Medrano, Identification of refractory weakly basic nitrogen compounds in a deeply hydrotreated vacuum gas oil and assessment of the effect of some representative species over the performance of a Ni–MoS$_2$/Y-Zeolite–Alumina catalyst in Phenanthrene Hydrocracking, Energy Fuels 32 (2018) 8715–8726.

[37] K. Zhang, J. Yu, S. Gao, C. Li, G. Xu, Understanding shale oil hydrotreatment with composition analysis using positive-ion mode atmospheric pressure photoionization fourier transform ion cyclotron resonance mass spectrometry, Energy Fuels 31 (2017) 1362–1369.

[38] E. Bae, J.G. Na, S.H. Chung, H.S. Kim, S. Kim, Identification of about 30 000 chemical components in shale oils by electrospray ionization (ESI) and atmospheric pressure photoionization (APPI) coupled with 15 T fourier transform ion cyclotron resonance mass spectrometry (FT-ICR MS) and a comparison to, Energy Fuels 24 (2010) 2563–2569.

[39] A.M. McKenna, J.M. Purcell, R.P. Rodgers, A.G. Marshall, Heavy petroleum composition. 1. Exhaustive compositional analysis of athabasca bitumen HVGO distillates by fourier transform ion cyclotron resonance mass spectrometry: a definitive test of the boduszynski model, Energy Fuels 24 (2010) 2929–2938.

[40] B.M. Ruddy, M. Huettel, J.E. Kostka, V.V. Lobodin, B.J. Bythell, A.M. McKenna, C. Aeppli, C.M. Reddy, R.K. Nelson, A.G. Marshall, R.P. Rodgers, Targeted petroleomics: analytical investigation of macondo well oil oxidation products from pensacola beach, Energy Fuels 28 (2014) 4043–4050.

[41] A. Gutiérrez, J.M. Arandes, P. Castaño, M. Olazar, A. Barona, J. Bilbao, Effect of space velocity on the hydrocracking of light cycle oil over a Pt–Pd/HY zeolite catalyst, Fuel Process. Technol. 95 (2012) 8–15, https://doi.org/10.1016/j.fuproc.2011.11.003.

[42] I. Hita, R. Palos, J.M. Arandes, J.M. Hill, P. Castaño, Petcoke-derived functionalized activated carbon as support in a bifunctional catalyst for tire oil hydroprocessing, Fuel process, Technol. 144 (2016) 239–247.

[43] D. van Herk, P. Castaño, M. Quaglia, M.T. Kreutzer, M. Makkee, J.A. Moulijn, Avoiding segregation during the loading of a catalyst-inert powder mixture in a packed micro-bed, Appl. Catal. A Gen. 365 (2009) 110–121.

[44] M. Moini, B.L. Jones, R.M. Rogers, L. Jiang, Sodium trifluoroacetate as a tune/calibration compound for positive- and negative-ion electrospray ionization mass spectrometry in the mass range of 100–4000 Da, J. Am. Soc. Mass Spectrom. 9 (1998) 977–980.

[45] P. Castaño, A. Gutiérrez, B. Pawelec, J.L.G. Fierro, A.T. Aguayo, J.M. Arandes, Effect of the support on the kinetic and deactivation performance of Pt/support catalysts during coupled hydrogenation and ring-opening of pyrolysis gasoline, Appl. Catal. A Gen. 333 (2007) 161–171.

[46] A.G. Marshall, R.P. Rodgers, Petroleomics: chemistry of the underworld, Proc. Natl. Acad. Sci. U. S. A. 105 (2008) 18090–18095.

[47] T. Kekäläinen, J.M.H. Pakarinen, K. Wickström, V.V. Lobodin, A.M. McKenna, J. Jänis, Compositional analysis of oil residues by ultrahigh-resolution fourier transform ion cyclotron resonance mass spectrometry, Energy Fuels 27 (2013) 2002–2009.

[48] J. Crepier, A. Le Masle, N. Charon, F. Albrieux, P. Duchene, S. Heinisch, Ultra-high performance supercritical fluid chromatography hyphenated to atmospheric pressure chemical ionization high resolution mass spectrometry for the characterization of fast pyrolysis bio-oils, J. Chromatogr. B. 1086 (2018) 38–46.

[49] A. Gaspar, E. Zellermann, S. Lababidi, J. Reece, W. Schrader, Characterization of saturates, aromatics, resins, and asphaltenes heavy crude oil fractions by atmospheric pressure laser ionization fourier transform ion cyclotron resonance mass spectrometry, Energy Fuels 26 (2012) 3481–3487.

[50] F. Handle, M. Harir, J. Füssl, A.N. Koyun, D. Grossegger, N. Hertkorn, L. Eberhardsteiner, B. Hofko, M. Hospodka, R. Blab, P. Schmitt-Kopplin, H. Grothe, Tracking aging of bitumen and its saturate, aromatic, resin, and asphaltene fractions using high-field fourier transform ion cyclotron resonance mass spectrometry, Energy Fuels 31 (2017) 4771–4779.

[51] P. Rathsack, M. Kroll, A. Rieger, R. Haseneder, D. Gerlach, J.U. Repke, M. Otto, Analysis of high molecular weight compounds in pyrolysis liquids from scrap tires using Fourier transform ion cyclotron resonance mass spectrometry, J. Anal. Appl.

[52] A.G. Marshall, R.P. Rodgers, Petroleomics: the next grand challenge for chemical analysis, Acc. Chem. Res. 37 (2004) 53–59.

[53] C.S. Hsu, C.L. Hendrickson, R.P. Rodgers, A.M. McKenna, A.G. Marshall, Petroleomics: advanced molecular probe for petroleum heavy ends, J. Mass Spectrom. 46 (2011) 337–343.

[54] R.C.Y. Ong, P.J. Marriott, A review of basic concepts in comprehensive two-dimensional gas chromatography, J. Chromatogr. Sci. 40 (2002) 276–291.

[55] S.-S. Cai, K.A. Hanold, J.A. Syage, Comparison of atmospheric pressure photo-ionization and atmospheric pressure chemical ionization for normal-phase LC/MS chiral analysis of pharmaceuticals, Anal. Chem. 79 (2007) 2491–2498.

[56] A.R. Payne, R.E. Whittaker, Low strain dynamic properties of filled rubbers, Rubber Chem. Technol. 44 (1971) 440–478.

[57] P.J. Becker, N. Serrand, B. Celse, D. Guillaume, H. Dulot, A single events micro-kinetic model for hydrocracking of vacuum gas oil, Comput. Chem. Eng. 98 (2017) 70–79.

[58] P. Castaño, A. Gutiérrez, I. Villanueva, B. Pawelec, J. Bilbao, J.M. Arandes, Effect of the support acidity on the aromatic ring-opening of pyrolysis gasoline over Pt/HZSM-5 catalysts, Catal. Today 143 (2009) 115–119.

[59] P. Castaño, B. Pawelec, A.T. Aguayo, A.G. Gayubo, J.M. Arandes, The role of zeolite acidity in coupled toluene hydrogenation and ring opening in one and two steps, Ind. Eng. Chem. Res. 47 (2008) 665–671.

[60] L. Xin, X. Liu, X. Chen, X. Feng, Y. Liu, C. Yang, Efficient conversion of light cycle oil into high-octane-Number gasoline and light olefins over a mesoporous ZSM-5 catalyst, Energy Fuels 31 (2017) 6968–6976.

[61] J. Xu, T. Huang, Y. Fan, Highly efficient NiMo/SiO$_2$-Al$_2$O$_3$ hydrodesulfurization catalyst prepared from gemini surfactant-dispersed Mo precursor, Appl. Catal. B Environ. 203 (2017) 839–850.

[62] M. Dorneles de Mello, F. de Almeida Braggio, B. da Costa Magalhães, J.L. Zotin, M.A.P. da Silva, Kinetic modeling of deep hydrodesulfurization of dibenzothiophenes on NiMo/alumina catalysts modified by phosphorus, Fuel Process. Technol. 177 (2018) 66–74.

[63] Y.S. Al-Zeghayer, P. Sunderland, W. Al-Masry, F. Al-Mubaddel, A.A. Ibrahim, B.K. Bhartiya, B.Y. Jibril, Activity of CoMo/γ-Al$_2$O$_3$ as a catalyst in hydrodesulfurization: effects of Co/Mo ratio and drying condition, Appl. Catal. A Gen. 282 (2005) 163–171.

[64] E. Rodríguez, G. Félix, J. Ancheyta, F. Trejo, Modeling of hydrotreating catalyst deactivation for heavy oil hydrocarbons, Fuel. 225 (2018) 118–133.

[65] O. Klimov, K. Nadeina, Y.V. Vatutina, E. Stolyarova, I. Danilova, E.Y. Gerasimov, I. Prosvirin, A. Noskov, CoMo/Al$_2$O$_3$ hydrotreating catalysts of diesel fuel with improved hydrodenitrogenation activity, Catal. Today 307 (2018) 73–83.

[66] E. Furimsky, F.E. Massoth, Hydrodenitrogenation of petroleum, Catal. Rev. 47 (2005) 297–489.

[67] M. Bachrach, T.J. Marks, J.M. Notestein, Understanding the hydrodenitrogenation of heteroaromatics on a molecular level, ACS Catal. 6 (2016) 1455–1476.

[68] M. Shao, H. Cui, S. Guo, L. Zhao, Y. Tan, Effects of calcination and reduction temperature on the properties of Ni-P/SiO$_2$ and Ni-P/Al$_2$O$_3$ and their hydro-denitrogenation performance, RSC Adv. 8 (2018) 6745–6751.

[69] E. Furimsky, Catalytic hydrodeoxygenation, Appl. Catal. A Gen. 199 (2000) 147–190.

[70] H. Jahromi, F.A. Agblevor, Hydrodeoxygenation of pinyon-juniper catalytic pyrolysis oil using red mud-supported nickel catalysts, Appl. Catal. B Environ. 236 (2018) 1–12.

[71] P. Arora, H. Ojagh, J. Woo, E. Lind Grennfelt, L. Olsson, D. Creaser, Investigating the effect of Fe as a poison for catalytic HDO over sulfided NiMo alumina catalysts, Appl. Catal. B Environ. 227 (2018) 240–251.

[72] D. Otyuskaya, J.W. Thybaut, V. Alexiadis, M. Alekseeva, R. Venderbosch, V. Yakovlev, G.B. Marin, Fast pyrolysis oil stabilization kinetics over a Ni-Cu catalyst using propionic acid as a model compound, Appl. Catal. B Environ. 233 (2018) 46–57.

[73] T. Szarvas, Z. Eller, T. Kasza, T. Ollár, P. Tétényi, J. Hancsók, Radioisotopic investigation of the oleic acid-1-$^{14}$C HDO reaction pathways on sulfided Mo/P/Al$_2$O$_3$ and NiW/Al$_2$O$_3$ catalysts, Appl. Catal. B Environ. 165 (2015) 245–252.

[74] N. Azizi, S.A. Ali, K. Alhooshani, T. Kim, Y. Lee, J.-I. Park, J. Miyawaki, S.H. Yoon, I. Mochida, Hydrotreating of light cycle oil over NiMo and CoMo catalysts with different supports, Fuel Process. Technol. 109 (2013) 172–178.

[75] R.M. Navarro, P. Castaño, M.C. Álvarez-Galván, B. Pawelec, Hydrodesulfurization of dibenzothiophene and a SRGO on sulfide Ni(Co)Mo/Al$_2$O$_3$ catalysts. Effect of Ru and Pd promotion, Catal. Today 143 (2009) 108–114, https://doi.org/10.1016/j.cattod.2008.08.038.